PATMOS-x Version 6.0: 40 Years of Merged AVHRR and HIRS Global Cloud Data

MICHAEL J. FOSTER,[a] CODA PHILLIPS,[a] ANDREW K. HEIDINGER,[b] EVA E. BORBAS,[a] YUE LI,[a] W. PAUL MENZEL,[a] ANDI WALTHER,[a] AND ELISABETH WEISZ[a]

[a] *Cooperative Institute of Meteorological Satellite Studies, University of Wisconsin–Madison, Madison, Wisconsin*
[b] *NOAA/NESDIS/STAR, Madison, Wisconsin*

(Manuscript received 3 March 2022, in final form 1 September 2022)

ABSTRACT: A new version of the PATMOS-x multidecadal cloud record, version 6.0, has been produced and is available from the NOAA National Centers for Environmental Information. A description of the processes and methods used for generating the dataset are presented, with a focus on the differences between version 6.0 and the previous version of PATMOS-x, version 5.3. The new version appears both to be more stable, with less intersatellite variability, and to have more consistent polar cloud detection, phase distribution, and cloud-top height distribution when compared against the MODIS EOS record. Improvements in consistency and performance are attributed to the addition of multidimensional variables for cloud detection, constraining cloud retrievals to radiometric bands available throughout the record, and the addition of data from the HIRS instrument.

SIGNIFICANCE STATEMENT: The PATMOS-x project produces multidecadal cloudiness records from polar-orbiting satellites. Version 6.0 combines imager and sounder data from 15 satellites and shows significant improvements in accuracy and stability.

KEYWORDS: Cloud cover; Cloud droplets; Cloud microphysics; Cloud retrieval; Clouds

1. Introduction

Clouds form primarily in updrafts created from convection, orographic lifting, frontal lifting, turbulence, and/or atmospheric mixing. They modulate surface temperature through absorption and emission of longwave radiation from Earth (a warming effect) and reflecting incoming shortwave radiation from the sun (a cooling effect). The height, opacity, and phase of clouds determine whether the net effect is one of heating or cooling. Clouds are generally associated with weather systems and on short time scales their formation is largely determined by synoptic events, but clouds also experience diurnal, seasonal, and interannual cycles. Interannual drivers of global cloudiness are large scale modes of variability, the most well known being El Niño–Southern Oscillation (ENSO). Strong El Niño and La Niña years are correlated with characteristic patterns of global cloudiness (Foster et al. 2014). In addition to affecting temperature, clouds store and transport atmospheric water and are an important component of the global hydrological cycle. Clouds are also gauges for hydrological-based hazards like drought, flooding, and wildfires. These factors mean that clouds play an essential role in the Earth climate system (Bony and Dufresne 2005; Boucher et al. 2014; Klein et al. 2017; Zelinka et al. 2016). Although records of cloud occurrence have been taken by human observers from weather stations and ships for several decades, satellites are increasingly chosen for cloud climate applications. This is due to measurement consistency, global coverage, and the ability to derive physical and optical properties of clouds as well as occurrence.

The Pathfinder Atmospheres–Extended (PATMOS-x) project is a collaboration between the National Oceanic and Atmospheric Administration (NOAA) and the Cooperative Institute for Meteorological Satellite Studies (CIMSS) at the University of Wisconsin–Madison. The primary goal of PATMOS-x is to develop satellite-based climate data records (CDRs) of atmospheric cloud properties. In addition, PATMOS-x CDRs include calibrated radiometric measurements and selected geolocation and surface products to facilitate use and allow for creation of new or value-added products. Applications for PATMOS-x have included climate monitoring (Foster et al. 2019), intercomparison studies (Karlsson and Devasthale 2018; Stubenrauch et al. 2012; Wu et al. 2014, 2017), climate research (Foster and Heidinger 2014; Zhong et al. 2016), solar energy research (Sengupta et al. 2018), cloud process studies (Rausch et al. 2010), hydrological studies (Nielsen et al. 2011), and the creation of new products (Zhao et al. 2013). PATMOS-x version 5.3 (Pv5.3) has been archived and made publicly available at the NOAA National Centers for Environmental Information (NCEI) since 2011 (Heidinger et al. 2014). It is derived from the Advanced Very-High-Resolution Radiometer (AVHRR). The AVHRR instrument has flown on the NOAA Polar Orbiting Environmental Satellite series (POES) since 1978 and the EUMETSAT Polar System (EPS) Meteorological Operational (MetOp) series since 2006. The High-Resolution Infrared Sounder (HIRS) is a 20-channel scanning infrared (IR) radiometer used for operational sounding also flown on these satellites. One of the major tasks for creating the next edition of PATMOS-x, version 6.0 (Pv6.0), has been collocating and interpolating the AVHRR and HIRS measurements into a single radiometric record. The purpose of this paper is to describe this process along with changes and improvements in Pv6.0.

Corresponding author: Michael J. Foster, mike.foster@ssec.wisc.edu

DOI: 10.1175/JCLI-D-22-0147.1

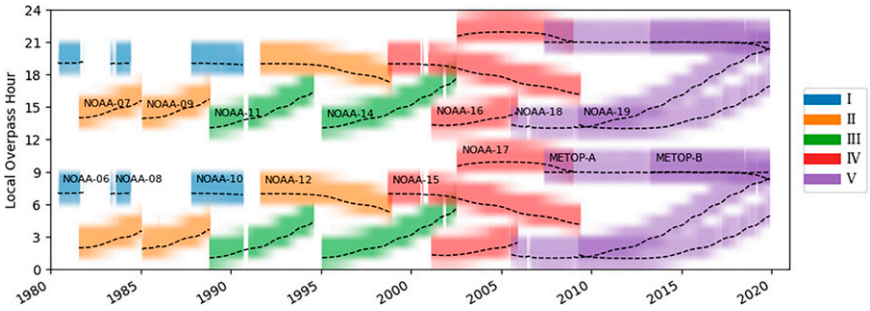

FIG. 1. Equatorial crossing time for NOAA POES and EUMETSAT MetOp satellites included in Pv6.0. Colors map to five periods of time that have distinct availability of radiometric bands. These periods will be discussed in section 2d.

Much of the basic information regarding the AVHRR and PATMOS-x data formats has been described in detail in Heidinger et al. (2014). Therefore, this article will focus on improvements between Pv5.3 and Pv6.0. Section 2 will describe the radiometric data used in Pv6.0 and the process used to merge the AVHRR and HIRS measurements along with quality assurance procedures. Section 3 will describe developments in the PATMOS-x retrieval algorithms since Pv5.3 and the addition of total precipitable water (TPW). Section 4 will compare results from Pv5.3 and Pv6.0 and assess improvements in the record stability with emphasis on cloud detection over polar regions, which is a known challenge for Pv5.3, and section 5 is for conclusions.

2. PATMOS-x input

PATMOS-x records are derived from the NOAA Polar Operational Environmental Satellites (POES) and EUMETSAT MetOp satellites. NOAA historically launched satellites in alternating evenly spaced orbits with the goal of achieving consistent global coverage. Satellites in the "morning" orbit cross the equator during the descending (southward) node at 0730 local time (LT). Satellites in this orbit include *NOAA-6*, *NOAA-8*, *NOAA-10*, *NOAA-12*, and *NOAA-15*. Satellites in the "afternoon" orbit cross the equator during the ascending (northward) node at 1330 LT. Satellites in this orbit include *NOAA-7*, *NOAA-9*, *NOAA-11*, *NOAA-14*, *NOAA-16*, *NOAA-18*, and *NOAA-19*. A third "mid-morning" orbit began with the launch of *NOAA-17* where it crossed the equator during the descending node at 1000 LT. The MetOp satellites are flown in this orbit with the equator overpass adjusted to 0930 LT. Figure 1 shows the equatorial crossing time of each satellite included in Pv6.0, color-coded by periods with distinct radiometric information. These periods and their significance to Pv6.0 will be discussed in more detail in section 2d. The longer a satellite remains operational the farther it drifts from its original orbit (Ignatov et al. 2004). This is particularly true for the early satellites, as the MetOp satellites are flown in controlled orbits. The drift creates an aliasing effect that must be addressed for applications such as trend detection and climate monitoring (Foster and Heidinger 2013). Pv5.3 included another satellite, *TIROS-N*, which flew from 1978 to 1981. It has not been processed for Pv6.0 because there were very few data available that met quality assurance parameters, which will be discussed in section 3. A third MetOp satellite, *MetOp-C*, was launched in 2018. It has not been included in Pv6.0 because it lacks a HIRS instrument.

a. AVHRR

PATMOS-x versions 5.3 and 6.0 use measurements from the Advanced Very High Resolution Radiometer (AVHRR; Cracknell 1997). The AVHRR is capable of recording raw counts in six spectral bands: channel 1 (0.63 μm), channel 2 (0.86 μm), channel 3a (1.6 μm), channel 3b (3.75 μm), channel 4 (11 μm), and channel 5 (12 μm). Several iterations of the AVHRR exist that result in different channels being available at different times in the record. The AVHRR/1 was flown on *NOAA-6*, *NOAA-8*, and *NOAA-10* and did not include channel 3a (1.6 μm) or channel 5 (12 μm). The AVHRR/2 was flown on *NOAA-7*, *NOAA-9*, *NOAA-11*, *NOAA-12*, and *NOAA-14* and added channel 5 (12 μm), and AVHRR/3 was flown on *NOAA-15*, *NOAA-16*, *NOAA-17*, *NOAA-18*, *NOAA-19*, and the MetOp satellites and added channel 3a (1.6 μm). The AVHRR/3 is limited to five simultaneous raw count measurements so switching occurs between channels 3a and 3b. This switching varies among the satellites. For *NOAA-17*, *MetOp-A*, *MetOp-B*, and *MetOp-C* channel 3a is on during the day and channel 3b is on at night. For *NOAA-15*, *NOAA-18*, and *NOAA-19* channel 3a was largely unused, whereas for *NOAA-16* channel 3a was used at launch but stopped in May 2003, after which channel 3b was used. This is important as cloud optical properties rely on a near-infrared (NIR) channel for retrieval, and the 1.6- and 3.75-μm bands retrieve different information.

AVHRR data come in several formats, but the one used for PATMOS-x is the global area coverage (GAC) format as it is the only format available globally throughout the AVHRR record. The AVHRR field of view is approximately 1.1 km at nadir for a single raw count measurement. GAC data are derived by averaging raw sensor counts from four of the five measurements along the central scan line of a 3 × 5 array, meaning the effective GAC spatial resolution is approximately 4 km at nadir and coarsens near the edge of the scan. The AVHRR lacks onboard visible calibration so for the visible (solar) channels (1, 2, 3a, and 3b) a vicarious intercalibration method is employed to improve consistency throughout the record. The calibration method uses simultaneous nadir overpasses (SNOs) for AVHRR to AVHRR

and AVHRR to Moderate Resolution Imaging Spectroradiometer (MODIS) as well as stable targets and is described in Heidinger et al. (2010) and Heidinger et al. (2002). Since those publications the calibration method has been updated to apply spectral band adjustments to make more consistent comparisons between satellites using SCIAMACHY (Scanning Imaging Absorption Spectrometer for Atmospheric Chartography) hyperspectral data (Scarino et al. 2016).

b. HIRS

Historically, the limited number of channels and inconsistent availability has made it difficult to differentiate clouds in challenging conditions (i.e., cold conditions over bright surfaces or at night). This has led to issues in polar cloud detection, optically thin cirrus height assignment, and intersatellite consistency. Pv6.0 addresses these issues by incorporating spectral information from the High-Resolution Infrared Sounder (HIRS). The HIRS is an atmospheric sounder that provides information on, among other things, water vapor and CO_2 absorption that the AVHRR lacks. Its 20 spectral bands comprise 1 visible, 7 shortwave IR, and 12 longwave IR channels. Like the AVHRR there have been several iterations of the HIRS instrument. The HIRS/2 and HIRS/3 instruments have an approximately 19-km field of view (FOV) at nadir, while the HIRS/4 increased the spatial resolution to 10 km. There have been changes in the bands available among the different versions of HIRS and some shifts in spectral response functions (SRFs) of existing bands. Section 2d will discuss these differences and the implications for Pv6.0. HIRS calibration includes applying SRF shifts to IR channels (Zhang et al. 2021).

c. AVHRR/HIRS merge methodology

The "imager plus sounder" (or imager/sounder) fusion method was originally developed to create missing absorption bands for the Visible Infrared Imaging Radiometer Suite (VIIRS) (Cross et al. 2013). Whereas a sensor like MODIS has multiple IR absorption bands, the current VIIRS imager has only IR window bands; that is, it does not have any CO_2 absorption bands (which are essential to retrieve cloud properties like height and phase, but also accurate soundings) or water vapor absorption bands. Weisz et al. (2017) demonstrated that an IR absorption band missing from an imager can be constructed by merging high-spatial-resolution imager data with high-spectral (but coarse spatial)-resolution sounder data.

The imager/sounder fusion process requires two steps [as described in Weisz et al. (2017)]. In the first step a nearest-neighbor search, specifically a multidimensional KD tree algorithm, on original high-spatial-resolution and low-spatial-resolution split-window 11- and 12-μm imager radiances is performed. In this case the "high spatial" radiance is an AVHRR pixel and the "low-spatial"-resolution imager radiances are created by geographically collocating each imager (AVHRR) pixel within a sounder (HIRS) FOV, and then averaging the radiance values within that FOV. The corresponding imager and sounder geolocation (latitude and longitude) information are used as additional predictors. This search finds, for each imager pixel, the low-FOV-resolution radiances (and geolocations) that best match the high-pixel-resolution radiances (and geolocations). Thus, the first step provides the indices of the (typically top five) sounder FOVs that are the closest in radiance and geolocation values of each imager pixel. In the second step, the average of sounder radiance data associated with the selected five FOVs is computed to provide the final fused product at imager pixel resolution. That means that the final radiance is an average of the sounder radiances—and which of the sounder FOVs are being averaged (for each imager pixel) depends solely on the imager radiances. It is noted that hyperspectral sounder data (e.g., CrIS) are first integrated over a selected SRF to produce a convolved radiance before the nearest-neighbor averaging is performed. These new fusion radiances can be created for any band (e.g., every MODIS band) and then be used to infer profile, cloud, and surface parameters; thus, heritage algorithms can be applied to the fusion radiances to ensure continuation of applications that require IR absorption bands.

In AVHRR/HIRS fusion AVHRR channels 4 and 5 are used in step 1 (together with AVHRR and HIRS latitude/longitude information), and the HIRS radiances (for each band) are being averaged during step 2. Figure 2 illustrates the AVHRR/HIRS fusion process, and Fig. 3 shows an example of original HIRS radiance (for a subset of an orbit) in comparison with the high-spatial-resolution AVHRR/HIRS fusion results for HIRS band 7 (centered at 13.7 μm). HIRS has a narrower swath than AVHRR, and the fusion process fills in the full AVHRR granule. Fusion data outside the original HIRS swath generally have greater uncertainty, and the water vapor channels are affected more than the CO_2 channels. There is a discussion of this issue in Weisz et al. (2017) (Figs. 5 and 6). For Pv6.0 this problem is somewhat ameliorated during the creation of the daily output file, which samples the orbit data to a 0.1° global grid. When orbits overlap the measurement closest to nadir is selected, thereby removing the pixels closest to the edge of scan.

d. Spectral availability throughout the record

Reasons for including HIRS channels include improving accuracy of cloud products and allowing for the same spectral information to be used throughout the record to improve consistency and stability. Figure 4 shows the different bands available throughout the record beginning with *NOAA-6* and ending with *MetOp-B*. Plotting of the central wavelength for each of the bands and instruments shows that some remain relatively stable while others experience noticeable shifts. Large shifts or those that trend in a certain direction can potentially cause false signals in climate records. To address this the AVHRR and HIRS bands were assessed for long-term stability and primary cloud retrievals were restricted to those bands that did not experience dramatic or trending intersatellite shifts. For the most part, available bands depend on the versions of AVHRR and HIRS instruments flown on each satellite. Transitions of note have been labeled with letters a–d in Fig. 4, described below:

a) The 12-μm band added with the introduction of AVHRR/2.
b) The 8.2-μm band replaced with the 12.5-μm band on the *NOAA-11* and *NOAA-14* HIRS/2 instruments (and thereafter on HIRS/3 and HIRS/4).

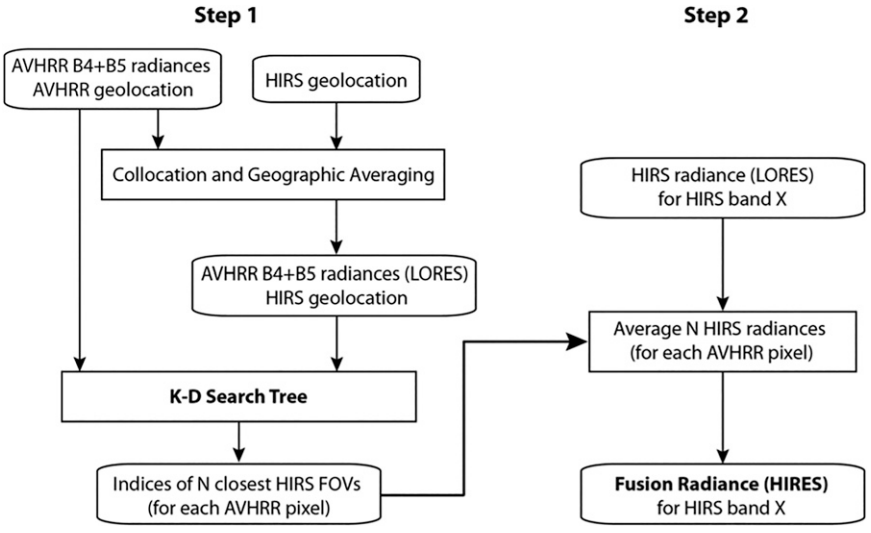

FIG. 2. Schematic of the AVHRR and HIRS data fusion process. HIRES and LORES refer to high spatial resolution and low spatial resolution, respectively.

c) HIRS channel 12 moved from 6.7 to 6.5 μm after the HIRS/2 to HIRS/3 transition.
d) A 1.6-μm band added after AVHRR/3 was introduced and the subsequent channel switching this created between AVHRR channels 3a and 3b.

Unique pairings of AVHRR and HIRS instruments, considering the 8.2- to 12.5-μm replacement, can be differentiated into five different periods, denoted by Roman numerals I to V in Fig. 4. Evaluation of these periods resulted in the following strategies for Pv6.0:

- The 12-μm band is no longer used for cloud mask and height retrievals because the AVHRR/1 does not include this channel.
- The HIRS 3.75-μm band is used when the AVHRR/3 is switched to measure the 1.6-μm band. This allows a 3.75-μm band to be available throughout the record.

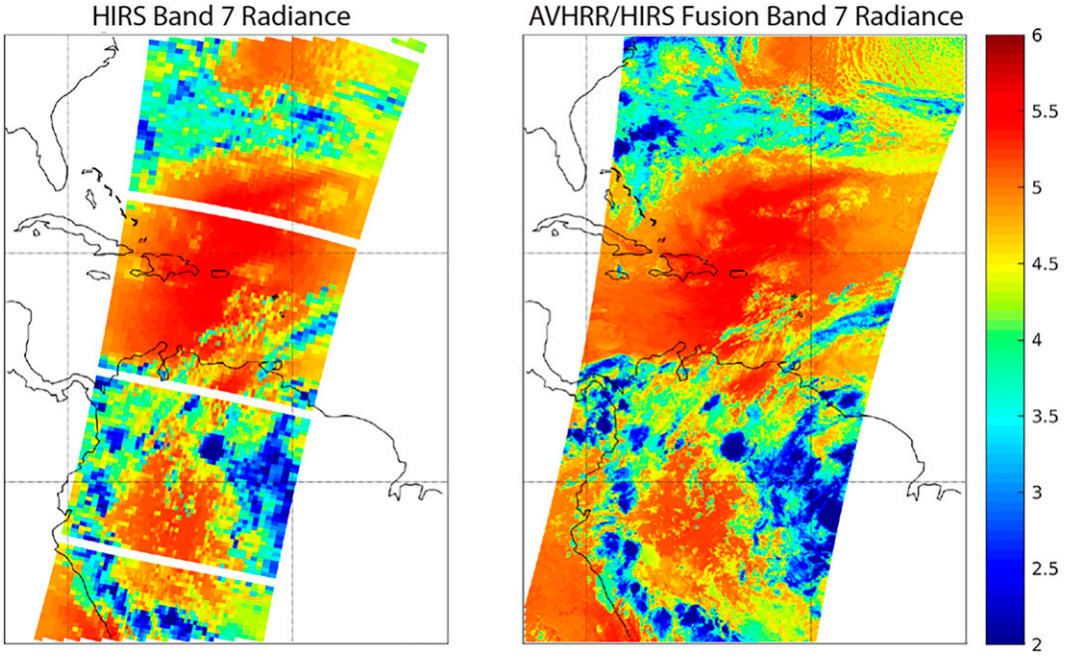

FIG. 3. (left) Original HIRS band 7 (13.7 μm) radiance and (right) the AVHRR/HIRS band 7 (13.7 μm) fusion radiances. The radiance unit is W m^{-2} ster^{-1} μm^{-1}. The white stripes in the left panel are due to a calibration procedure used by HIRS.

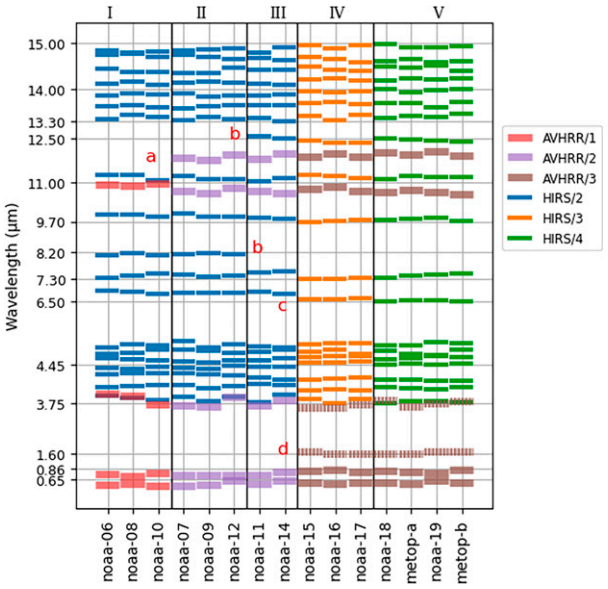

FIG. 4. Band availability and central wavelength for each AVHRR and HIRS instrument included in Pv6.0. Roman numerals represent periods with distinct AVHRR or HIRS version and band availability pairings (e.g., period II pairs HIRS/2 and AVHRR/2 with the 8.20-μm band). Lowercase letters mark start and stop points of band availability. Hashed AVHRR/3 bars indicate switching between 1.60- and 3.75-μm bands. Lowercase letters a to d mark significant shifts in radiometric information.

- The shift from 6.7 to 6.5 μm in HIRS channel 12 caused noticeable differences in cloud detection, so HIRS channel 11, 7.3 μm, was chosen instead (Liu et al. 2004).
- The 0.63-, 0.86-, 3.75-, 7.3-, 11.0-, and 13.3-μm bands are available and reasonably stable throughout the record, so cloud detection and height assignment are restricted to modes that operate with these bands.
- The integrated layer and total column moisture products are not subject to the same band restrictions, as these products were developed separately from the cloud products.

3. PATMOS-x output

PATMOS-x outputs dozens of atmospheric, surface, and ancillary data fields. However, the primary mission of PATMOS-x is detecting and characterizing atmospheric clouds. To this end most of the cloud properties in PATMOS-x are produced by one of three algorithms. The first is cloud detection and phase characterization, the second is top height assignment, and the third is cloud optical property retrieval. The fundamental architecture of these three algorithms has remained similar between Pv5.3 and Pv6.0 (except for cloud phase), but there have been several developments that will be discussed in the following sections.

a. Cloud mask and phase

PATMOS-x employs the NESDIS Enterprise Cloud Mask (ECM). The ECM represents an evolution of the naïve Bayesian cloud detection algorithm used for the previous version of PATMOS-x and described in Heidinger et al. (2012). The ECM continues to be trained using the cloud phase product from the NASA *CALIPSO*/CALIOP Cloud Layer Product. The CALIOP cloud phases distinguish between clear, water clouds, and ice clouds. These categories are used in the ECM to generate the probability of each pixel being either clear, a water cloud, or an ice cloud. The final probability of being cloudy is one minus the probability of clear. The Pv6.0 ECM can use one-, two-, or three-dimensional classifiers while Pv5.3 was limited to single dimensions. In addition, the ECM now uses a selective decision optimization method. This process begins by identifying the best performing classifier, and then identifying the classifier that improves the performance the most in combination with the first classifier. This process continues until no further performance gain is achieved by adding additional classifiers. One of the main advantages of using an optimization is that correlation between classifiers is reduced while increasing the overall performance. The optimization is performed separately for each surface type because the relative correlations of the classifiers will vary with surface type. The surface types used in the ECM remain unchanged from those defined in Heidinger et al. (2010). Table 1 lists those classifiers used for each surface type after the application of optimization process.

Whereas in Pv5.3 the naïve Bayesian cloud mask was only used to determine cloud probabilities, in Pv6.0 it is also used to determine cloud phase. As stated above, the ECM is trained using the CALIOP cloud phase and generates the probabilities of each pixel being an ice or water cloud. In Pv6.0, these probabilities are used to first estimate the phase (ice or water) of cloudy pixels (cloud probability > 0.5). The cloud probability is then used as an uncertainty estimate for clear pixels (one minus cloud probability is used for cloudy pixels). In addition to the cloud probability uncertainty, Pv6.0 now makes a cloud phase uncertainty using a similar formula and has a maximum value of 50%. Once the phase is determined, thresholds on the cloud opaque temperature and cloud 11-μm emissivity referenced to the tropopause are used to compute the cloud types. The values and meanings of the cloud types are identical from the previous version of PATMOS-x, with the exception of the overlap type. In Pv6.0, the overlap type is computed for pixels that initially have a cirrus type classification but have a phase uncertainty greater than 10%.

Being a naïve Bayesian approach, the ECM uses a prior value in its formulation. The prior values for the ECM are computed from 9 years of Level 3 *CALIPSO*/CALIOP Global Energy and Water Cycle Experiment (GEWEX) cloud product (Stubenrauch et al. 2012). Daytime, nighttime, and day-night mean data are computed and saved separately for each grid and month. To fill missing values after multiyear averages are derived, a simple spatial averaging method is applied by assigning the average of a 9×9 box surrounding a missing value grid. This approach is iterated until all missing values are filled.

7.3-μM LUT CORRECTION

During the preparation of Pv6.0 it was discovered that there was a change in the channel 12 spectral response function

TABLE 1. Pv6.0 cloud mask classifiers and applicable surface types. Multidimensional classifiers are separated by dimension (e.g., Dim1 and Dim2).

Classifier	Calculation	Deep water	Shallow water	Unfrozen land	Frozen land	Arctic	Antarctic	Desert
Bt11_btd13373	Dim1: 11.0 μm Dim2: 13.3 − 7.3 μm				ON	ON		
Bt11_btd3811_day	Dim1: 11.0 μm Dim2: 3.75 − 11.0 μm			ON	ON	ON	ON	ON
Bt11_btd3811_night	Dim1: 11.0 μm Dim2: 3.75 − 11.0 μm		ON	ON	ON	ON	ON	ON
btd11133	11.0 − 13.3 μm	ON					ON	
btd1173	11.0 − 7.3 μm				ON	ON	ON	
dbt11max3 × 3	Max 11.0 μm − mean 11.0 μm (3 × 3 pixel array)	ON	ON	ON				ON
drefl065min3 × 3	Mean 0.65 μm − min 0.65 μm (3 × 3 pixel array)	ON					ON	
Logbt11std_logrefl065std	Dim1: Log of the std. dev. of the 11 μm BT (3 × 3 pixel array) Dim2: Log of the std dev of the 0.65 μm reflectance (3 × 3 pixel array)				ON	ON	ON	
Logzopa_topa_logbt11std	Dim1: Log of the opaque cloud height Dim2: Opaque cloud temperature Dim3: Log of the std dev of the 11 μm BT (3 × 3 pixel array).	ON	ON	ON		ON	ON	ON
refrat086065	0.86 μm/0.65 μm	ON	ON	ON	ON			ON

between HIRS/2 and HIRS/3. For the sake of intersatellite consistency, the water vapor channel used for cloud detection was changed to the more stable channel 11, having a central wavelength of approximately 7.3 μm. The atmosphere is more transparent in this channel; the weighting function peaks at a lower altitude. Small intersatellite shifts in the 7.3-μm band still existed, which caused an observable bias in the polar cloud record. To account for this, an adjustment was made at the level of cloud classifier lookup table values. Typically, lookup tables used in the naïve Bayes cloud detection are shared among all satellites, but for the 7.3-μm classifier this is done for each satellite individually. This was done by mapping table indices to quantiles of the satellite's overall distribution and then interpolating to the inverse-CDF of a reference satellite's distribution. For example, if the *NOAA-14* 7.3-μm BTD fell in the 25th percentile of *NOAA-14* values, the lookup table value would be that of the 25th percentile of *NOAA-19* values. This method was highly effective at removing most of the generation shift in cloud fraction, but a small generational shift remains in the wintertime Arctic.

Polar cloud detection

One of the primary goals of including HIRS radiometric information in Pv6.0 was to address the shortcomings in Pv5.3 polar cloud detection. To this end studies were conducted to see how and where the introduction of the 7.3- and 13.3-μm channels affected the cloud mask. Figure 5 shows cloud detection in configurations with and without these channels. Figure 5a shows the difference in cloud detection in Pv6.0 and Pv5.3 without the use of any HIRS channels, meaning these differences are due to other changes in the Pv6.0 cloud mask. These primarily include the addition of 2D and 3D classifiers, the constraint of only using bands available throughout the record, and the addition of updated prior values for the naïve Bayesian scheme. For this study every 30th day of Pv6.0 was processed without HIRS, which can be seen in the noisiness of Fig. 5a. Generally, cloudiness increases over ice-free oceans, high altitudes, and northern landmasses. Cloudiness decreases over tropical and midlatitude landmasses and polar regions. The addition of the 7.3-μm band in Fig. 5b shows cloudiness reductions in high-latitude oceans and landmasses and some of the Antarctic. The addition of the 13.3-μm band in Fig. 5c produces sharp decreases in cloudiness in the Antarctic and Greenland. This is not unexpected as Antarctica and Greenland are paired as a single surface type when training the naïve Bayesian scheme. This suggests that the use of different surface types for training the cloud mask may introduce regional inconsistencies. Figure 5c also shows increasing midlatitude marine cloudiness. Figure 5d shows Pv6.0 − Pv5.3 with all bands included. The pattern is like Fig. 5a with primary

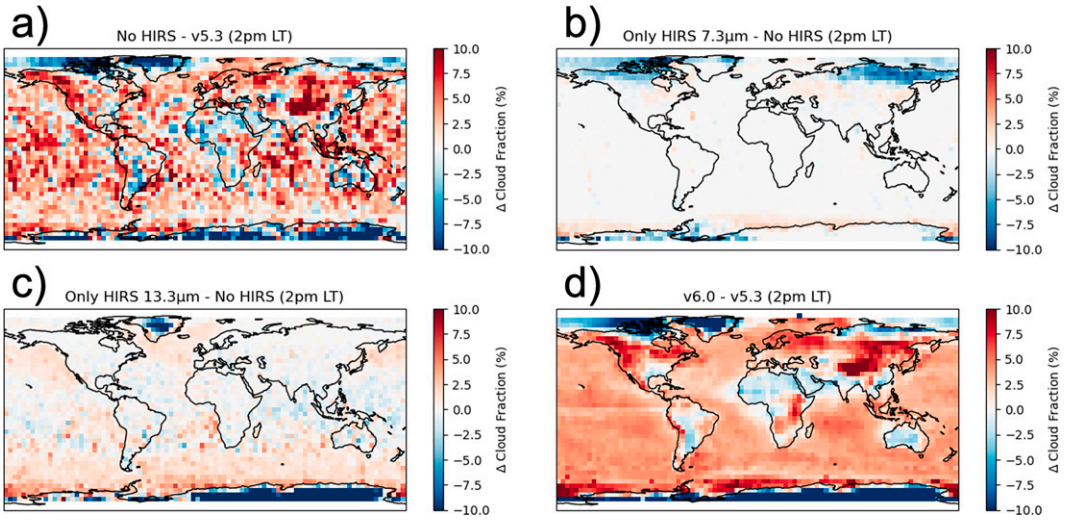

FIG. 5. Changes in cloud detection. (a) Difference in average cloud fraction between the Pv6.0 cloud mask run without any HIRS bands and Pv5.3 at 1400 local time. (b) Contributions of the 7.3-μm channels. (c) Contribution of the 13.3-μm band. (d) Overall difference between Pv6.0 and Pv5.3. Data were created by processing every 30th day of the record.

differences seen in high latitudes, suggesting that the HIRS channels are primarily contributing to cloud detection in these regions.

b. *Cloud height assignment*

Cloud height is retrieved by the NOAA Algorithm Working Group (AWG) Cloud Height Algorithm (ACHA) component of processing (Heidinger and Pavolonis 2009). ACHA is an optimal estimation (Rodgers 1976) routine that supports many combinations of channels as input. Since Pv5.3, several ACHA developments have occurred:

- Lower-level cloud-top height is now retrieved when multilayer clouds are present (i.e., cirrus over water clouds). The presence of multilayer clouds is based on the upstream cloud type algorithm. Additionally, thin ice (cirrus) cloud-top height is retrieved in a multilayer system. If the estimated lower-level cloud height is close to the surface (<1 km), it is considered single-layer cloud and no lower-level retrievals are reported.
- ACHA generates ice cloud probability as an internal variable, which allows flexibility to modify input cloud type to optimize performance.
- Clouds are processed in different orders, with single-layer clouds processed before multilayer clouds, and thick ice clouds before thin cirrus. In this way thick cloud tops can be used as a priori values for nearby thin clouds. In Pv5.3 a simple nearest-neighbor averaging scheme is used for this purpose, but in Pv6.0 a KD-tree method has been introduced for retrieving thin cirrus, as well as multilayer cases. This was introduced in part to address the frequent occurrence of cirrus generated from cold thick cloud-top outflow, as well as a relatively uniform spatial distribution of ice cloud tops (Heidinger et al. 2019).
- A secondary cloud height is derived using an approach similar to the CO_2 slicing method (Menzel et al. 2008). This retrieval is unsuitable for climate trend analysis due to significant changes to the HIRS response functions in the 13.9- and 14.2-μm bands, so it is included as a separate output field but is not used as an a priori value for the primary ACHA retrieval.

In Pv5.3 ACHA ran using 11- and 12-μm bands (11_12 mode) for AVHRR/2 and AVHRR/3 and 11 μm only for AVHRR/1. For Pv6.0 the ACHA mode has been changed to use 11- and 13.3-μm bands (11_133 mode) for all satellites. To characterize this, a study was performed with two satellites from the NASA A-Train series: *Aqua* MODIS and *Cloud–Aerosol Lidar and Infrared Pathfinder Satellite Observation* (*CALIPSO*). ACHA was run in 11_12 and 11_133 modes using MODIS bands and collocated with CALIPSO/Cloud–Aerosol Lidar with Orthogonal Polarization (CALIOP) (Winker et al. 2009) V4–20 cloud layer products. Approximately 29 000 collocated height retrievals from a single day (13 June 2019) were used. Performance was compared for liquid versus ice phase and optically thin versus thick clouds, using a cloud optical depth threshold of 0.4. Overall, the 11_133 mode performed better than the 11_12 mode with cloud top temperature uncertainty relative to *CALIPSO*/CALIOP (defined as the square root of the sum of squares of accuracy and precision) being 1.6 K lower. There was variation depending on phase and thickness. The 11_133 mode average uncertainty was 1.5 K lower for thick clouds and 2.3 K lower for thin clouds. In addition, average uncertainty was 3.3 K lower for thick ice phase clouds and no change was found for thick liquid phase clouds. Accuracy and precision differences were also seen between the two modes. Average precision was 7.9 K for 11_12 mode and 6.5 K for 11_133 mode. Average accuracy was −2.0 K for 11_12 mode and −0.3 K for 11_133 mode. The 11_133 mode produced

more accurate and precise results than the 11_12 mode with most of the improvement associated with ice phase clouds.

c. Cloud optical properties

The Daytime Cloud and Optical and Microphysical (DCOMP; Walther and Heidinger 2012) retrieval is based on the bispectral approach introduced by Nakajima and King (1990). Cloud optical properties retrieved include the following products: cloud optical depth (COD), cloud effective radius (REF), and cloud emissivity. It is accomplished using measurements in at least two channels, one nonabsorbing and one weakly absorbing wavelength. The primary information of optical thickness lies in the visible window channel. The absorption channel provides additional information on effective radius and indirectly helps to correct optical thickness estimates for differences in forward-scattering due to variable particle size. Two DCOMP modes alternated within the dataset. Most satellites use the AVHRR 3.75-μm DCOMP mode for daytime cloud optical properties. *MetOp-A*, *MetOp-B*, *NOAA-16*, and *NOAA-17* use the AVHRR 1.6-μm DCOMP mode when it is available. The effect is not generally noticeable in COD. However, REF is significantly affected when using the 1.6 μm since the vertical penetration in the cloud is different for different wavelengths. Since Pv5.3, DCOMP changes include the following:

- Clear sky in DCOMP-processed regions reports values of zero for COD while nighttime and DCOMP retrievals that failed to converge are reported as "NaN." This makes physical sense, since optical thickness of zero is in the defined valid range. In contrast, the REF is not defined if there is no cloud in the observation path and will be reported as "Missing" for all those pixels. This also prevents confounding changes in DCOMP success rate with changes in cloudiness.
- An IR-based retrieval for COD is used as an a priori for the retrieval of very thin ice clouds. While the information skill for thin clouds (up to COD of 8) is limited in comparison to thicker clouds, an IR method provides more reliable results. DCOMP uses the IR result as an a priori, which get high weight in the a priori covariance matrix for thin clouds. The optimal estimation inversion technique regulates this process by setting the weighting accordingly with higher weights from IR measurement for very thin clouds.

d. Total precipitable water

The moisture retrieval algorithm is a clear-sky synthetic regression adopted from the operational GOES and MODIS (MOD07) algorithm (Seemann et al. 2003, 2008). It provides moisture properties at AVHRR spatial resolution over land and ocean for both day and night from combined HIRS and AVHRR data. A clear-sky regression relationship has been calculated from a SEEBOR global training radiosonde-based profile dataset (Borbas et al. 2005) between the temperature, moisture, and ozone atmospheric profiles and the brightness temperatures (BTs) of the 11 HIRS channels (2–12) and AVHRR split-window 11- and 12-μm bands. The HIRS + AVHRR moisture products include total column precipitable water (TPW) and three atmospheric layers of humidity—low (surface to 680 hPa), middle (680–440 hPa), and high (<440 hPa)—calculated by integrating the retrieved moisture atmospheric profiles. A high-spatial-resolution surface emissivity database differentiates surface emission and atmospheric moisture absorption (Seemann et al. 2008). The Radiative Transfer for TIROS Operational Vertical Sounder (RTTOV) version 11 (Saunders et al. 2018) forward model is used to calculate synthetic clear-sky brightness temperatures over areas identified as clear by the cloud mask. Regression coefficients are provided for the NOAA and MetOp satellites with and without (for validation purposes) the SRF adjustments (Zhang et al. 2021).

4. Performance

Here we present an analysis that focuses on how cloud retrievals have changed between Pv5.3 and Pv6.0, including comparisons against other cloud records. These include the Suomi National Polar-Orbiting Partnership (SNPP) Visible Infrared Radiometer Suite (VIIRS) Atmosphere Level 3 (L3) Cloud Properties product (CLDPROP_M3_VIIRS_SNPP; Platnick et al. 2019), the MODIS Atmosphere L3 monthly global product (MOD08_M3 and MYD08_M3, heretofore known as MODIS C6.1; Platnick et al. 2015), and the *CALIPSO*/CALIOP GEWEX lidar L3 cloud product (Stubenrauch et al. 2012). The *CALIPSO* product uses an active lidar for cloud detection and is considered a benchmark for the passive imagers. Finally, this analysis uses a version of PATMOS-x that was processed with measurements from *Aqua* and *Terra* MODIS (PxMOD). PxMOD advantageously runs the same set of algorithms as Pv6.0 but with a larger set of channels on orbit-controlled satellites. These records leverage satellites with more spectral information that experience little drift and do not rely on multiple generations of sensors for consistency. The disadvantage is they do not extend back into the 1980s and 1990s. Cloudiness is the first product examined and warrants the most attention as cloud detection affects subsequent retrieval of cloud properties and uses all of the bands available throughout the record.

a. Cloudiness

Figure 6 shows time series of global cloud fraction (CF) for Pv5.3 and Pv6.0, color-coded by satellite. The seasonal and drift correction was accomplished by backfitting a generalized additive model (GAM) for each $1^\circ \times 1^\circ$ grid box. The process is performed for water and ice phase clouds and the results are added to produce total cloudiness. The model defines the monthly observed cloudiness as the sum of a climatological cloudiness for the month x "local hour," a quarter-year anomaly, and noise. The periodic 2D table of month and hour cloudiness is linearly interpolated to fill missing elements and smoothed with a 1D Gaussian filter [standard deviation (std dev) = 1] along the hour axis only. Quarter-year anomalies are smoothed with a 1D Gaussian filter (std dev = 0.5). Two iterations of backfitting are used. The quarter-year anomaly fit is added to the climatological cloudiness fit, averaged over all months and hours, to produce the black line in Fig. 7. Global cloudiness increases by about 3% from Pv5.3 to Pv6.0. Both records show general downward trends in global

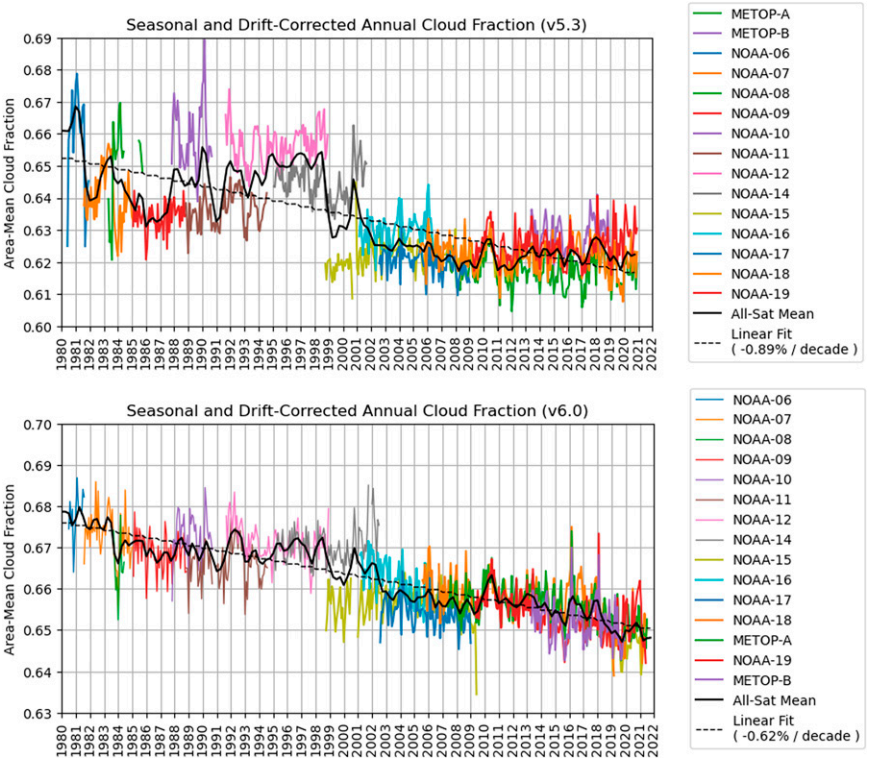

FIG. 6. Seasonal drift-corrected global cloud fraction time series for (top) Pv5.3 and (bottom) Pv6.0. Individual satellites are color-coded. The thick black line is the all-satellite mean and the dashed black line represents the linear fit.

cloudiness over the 40-yr period. For Pv5.3 the trend is −0.89% decade^{-1} while for Pv6.0 it is −0.62% decade^{-1}. Figure 6 shows a noticeable improvement in consistency and stability relative to Pv5.3, driven by a reduction in interannual and intersatellite variability. This can be attributed to improvements in cloud detection (refer to the cloud mask section above) and using the same bands throughout the record in Pv6.0. Spectral shifts in the 13.3-μm channel over the course of the record likely contribute to the negative trend, with the most apparent discontinuity occurring during the transition from *NOAA-14* to *NOAA-15* (1998–2002). A sensitivity study was performed to remove the effects of the 13.3 (not shown), and a small negative trend was still found. However, examination of the MODIS C6.1 record shows a slight increase in cloudiness over the course of its (shorter) record, suggesting further analysis may be warranted.

In Pv5.3 the morning orbit satellites, *NOAA-6*, *NOAA-8*, and *NOAA-10* (1980–90), show significantly higher cloudiness than the afternoon orbit satellites flying during the same period. These satellites comprise the band availability of period I as identified in Fig. 4. This period flies the AVHRR/1 and is missing a 12-μm band. In Pv5.3 the 12-μm band was used in the cloud mask when available, whereas for Pv6.0 only bands available throughout the record are used. In this case the larger negative trend in Pv5.3 can be attributed in part to the lack of a 12-μm band causing higher CF from period I satellites early in the record. Discontinuities between *NOAA-12* and *NOAA-11* and *NOAA-14* (1991–98) are reduced in Pv6.0, though others still exist. For example, a discontinuity occurs between *NOAA-14* and *NOAA-15* (1999–2002), which may be in part due to a shift in the 13.3-μm central wavelength (see Fig. 4). These differences tend to be small and regionally dependent but might need to be considered for certain applications.

When compared against other cloud products Fig. 7 shows that zonally averaged cloudiness is reasonably consistent among records. Antarctic cloudiness shows the largest variability and differences among records. Relative to CALIOP GEWEX L3, Pv5.3 detects more clouds while MODIS C6.1, PxMOD, Pv6.0, and SNPP VIIRS M3 detect less. Pv5.3 favorably agrees with CALIOP from 30° to 60°S and detects fewer clouds in the midlatitudes. SNPP VIIRS M3 agrees best with CALIOP in the tropics. Pv6.0 and PxMOD show the largest positive bias from 30° to 60°. Not surprisingly Pv6.0 is most like PxMOD. The largest differences between the two occur between 30° and 50°N and between 10° and 30°S. In both cases Pv6.0 detects more cloud than PxMOD.

b. *Cloud-top temperature*

Figure 8 shows cloud-top temperature (CTT) distributions for each of the satellites in Pv5.3 and Pv6.0 along with MODIS C6.1. For Pv5.3, CTT was retrieved using the 11- and 12-μm ACHA mode, except for *NOAA-6*, *NOAA-8*, and *NOAA-10* where the

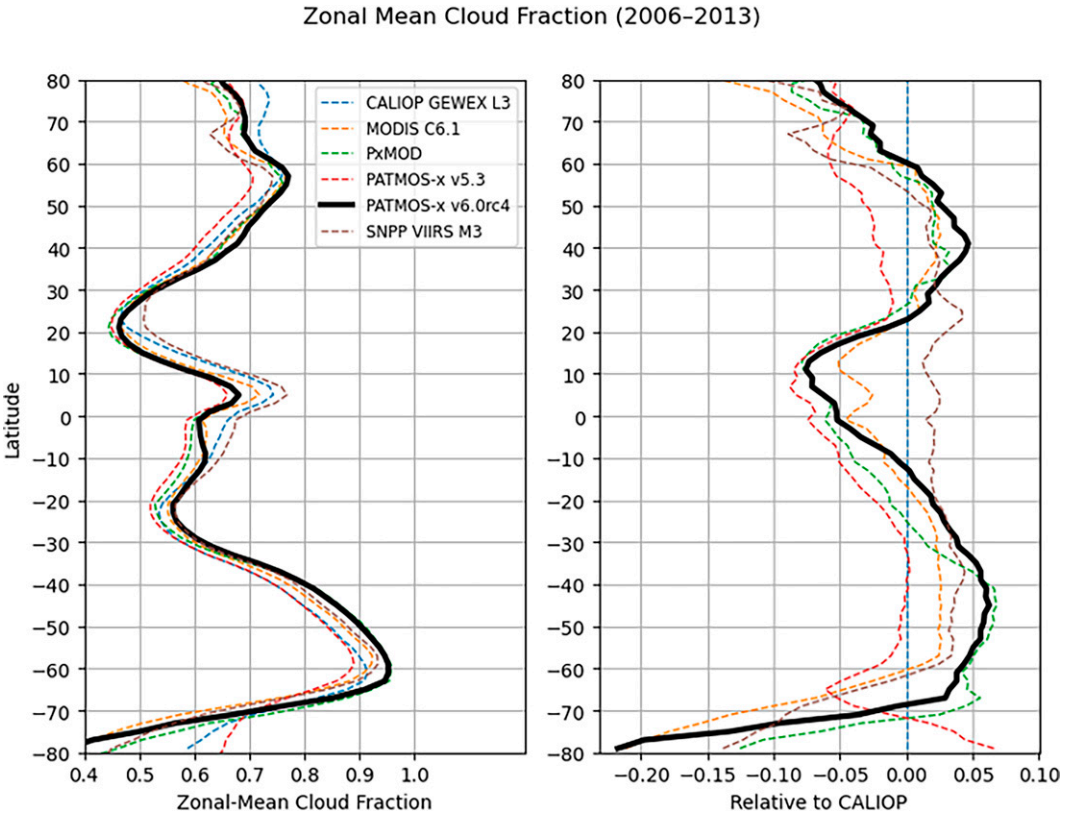

FIG. 7. Zonal-mean CF as reported for several long-term cloud records. (left) Zonally averaged CF between 2006 and 2013. (right) Differences relative to the CALIOP GEWEX L3 record.

12-μm channel was unavailable and therefore an 11-μm-only retrieval was used. This affects the distribution of CTT and these three satellites can be seen as outliers in Fig. 8 (left panel). There is also a prominent differentiation between the ice and liquid phase CTTs in Pv5.3, which causes disagreement with MODIS C6.1, which shows a smoother transition between phases. In Pv6.0 ACHA is run using the 11- and 13.3-μm modes, which are available for all satellites. This removes the outliers and brings the CTT distribution more in line with MODIS C6.1. The use of a carbon dioxide absorption channel creates some sensitivity to the spectral response function for each satellite, which can be seen in the distribution peaks. Peaks in several of the later satellites occur at a lower frequency and slightly colder temperature than the earlier satellites. As mentioned in section 4c, the 13.3-μm SRF shifts over the course of the record contribute to this, but there may also be changes due to the steady increase of carbon dioxide over the course of the record, as a small decreasing trend in 13.3-μm brightness temperatures was observed during the channel stability assessment not solely explained by shifts in SRFs. Further analysis of this phenomenon is warranted. This is not seen in Pv5.3 where the window channels experience minimal absorption.

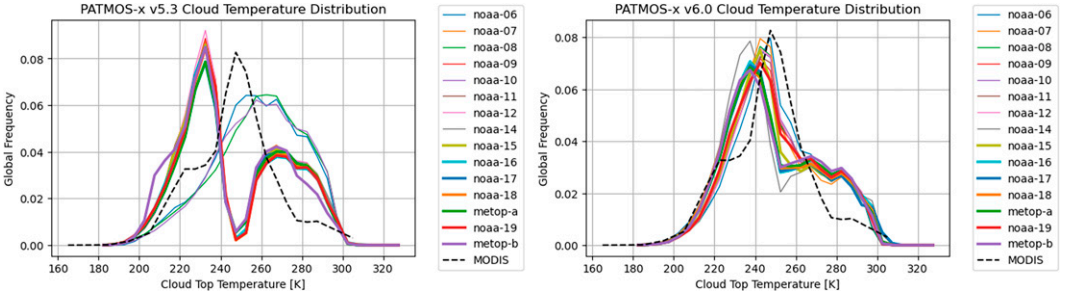

FIG. 8. ACHA cloud-top temperature comparison between (left) v5.3 and (right) v6.0.

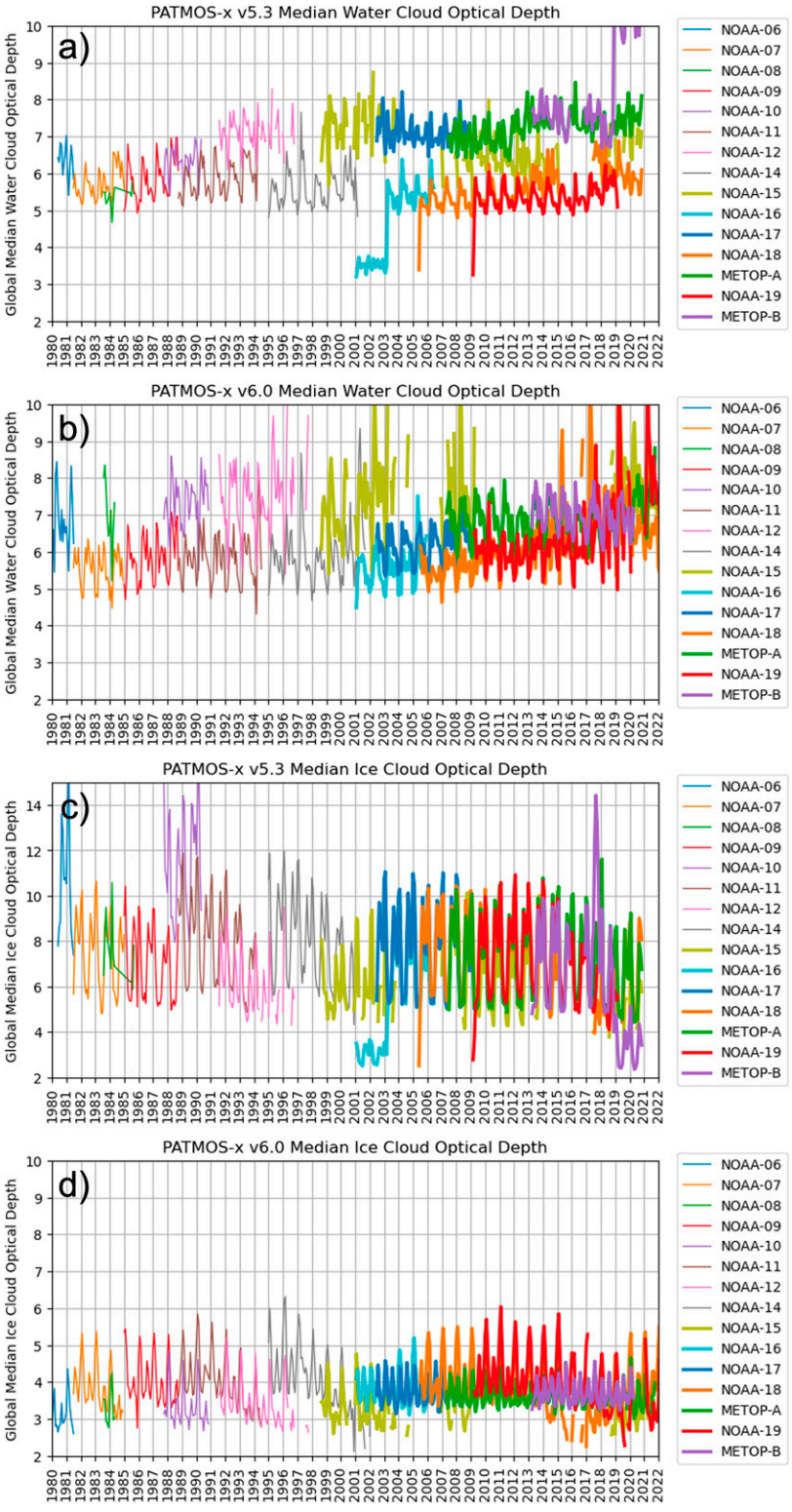

FIG. 9. Comparison of cloud optical depth for Pv5.3 and Pv6.0. Time series of median cloud optical depth are shown for (a) Pv5.3 water, (b) Pv6.0 water, (c) Pv5.3 ice, and (d) Pv6.0 ice.

c. Cloud optical depth and effective radius

Figure 9 shows median COD time series for water and ice clouds for each satellite in Pv5.3 and Pv6.0. Unlike the cloud mask and ACHA algorithms, the same set of spectral bands is used for the DCOMP retrievals. Consequently, differences in COD and REF are largely driven by cloud detection. For water clouds Pv6.0 provides some improvement in intersatellite stability, although the afternoon and morning orbits are clearly delineated since low-level clouds are more impacted by diurnal cycles of surface heating and cooling. The satellites that use the 1.60 DCOMP mode (*NOAA-17*, *MetOp-A*, *MetOp-B*, and the beginning of *NOAA-16*) retrieve more optically thin clouds. For Pv5.3 there are anomalous COD values at the beginning of the *NOAA-16*, *NOAA-18*, and *NOAA-19* records. The sudden shift in the *NOAA-16* record coincides with the switching from 1.60 to 3.75 μm. This suggests that *NOAA-18* and *NOAA-19* may have briefly used the 1.60-μm channel but does not explain why the initial values are so low. This difference is not seen in Pv6.0, suggesting the cause is the 1.60-μm channel being used for cloud detection in Pv5.3. This channel is not used in the Pv6.0 cloud mask (see Table 1).

For ice clouds Pv5.3 has larger median values and more variability; *NOAA-6* and *NOAA-10* are outliers and *MetOp-B* shows some anomalous behavior near the end of the record. In Pv6.0 the median values of ice COD are smaller and exhibit decreased magnitude of seasonal variability. This coincides with an overall increase in detected Pv6.0 cloud seen in Figs. 6 and 7 occurring primarily over ice-free oceans. The smaller values are due to increased detection of optically thin cirrus.

Figure 9 suggests the use of the 1.6-μm versus 3.75-μm band in the cloud optical property retrievals have relatively little effect on COD, as differences are seen primarily for optically thin clouds. This is not the case for REF, as the choice of NIR channel affects the effective cloud depth being measured. Differences in the distributions for satellites using the 1.6-μm versus 3.75-μm band for DCOMP retrievals are apparent, with the 1.6-μm satellites peaking near 15 μm and 3.75-μm satellites peaking near 10 μm. The 1.6-μm satellites also have a greater frequency of clouds with REF greater than 25 μm. *NOAA-16* shows a distribution between the 1.6- and 3.75-μm satellites that can be explained by switching from the 1.6- to 3.75-μm band, like what was seen for COD. For Pv5.3 the distribution of *NOAA-16* also shows anomalous spikes near 12 and 24 μm. Inspection of *NOAA-16* found scenes with nonphysical REF retrievals suggesting a bug in the processing not previously recorded. The time series in Fig. 10 shows median REF time series for Pv5.3 and Pv6.0 for water and ice clouds. The intersatellite consistency shows some improvement from Pv5.3 to Pv6.0, particularly for the 1.6-μm satellites, likely due to cloud detection and the lack of the 1.6-μm cloud mask classifiers in Pv6.0. For ice clouds the divergence between *NOAA-12* and *NOAA-14* is reduced and there appears to be less spread among *NOAA-15*, *NOAA-18*, and *NOAA-19* in the later record. Pv6.0 has a reduced median ice cloud REF for the 1.6- and 3.75-μm satellites, suggesting that the increased detection of thin cirrus corresponds with smaller particle sizes.

5. Conclusions

Polar cloudiness decreases in Pv6.0 where Pv5.3 contains high uncertainty. This can be attributed to improved cloud detection through the introduction of 2D and 3D classifiers, updated prior values for the naïve Bayesian detection scheme, and the introduction of the HIRS 7.3- and 13.3-μm bands. These changes make Pv6.0 agree better with more modern sensors (e.g., MODIS and VIIRS), but it is difficult to validate polar cloudiness with certainty.

Addition of the HIRS 13.3-μm channel for height retrieval removes the satellite outliers in the distribution of cloud-top temperatures due to the lack of a 12-μm channel in the AVHRR/1. It also produces distributions more in line with MODIS C6.1. However, the use of a carbon dioxide absorption channel seems to introduce some intersatellite sensitivity to the 13.3-μm spectral response function. A study comparing MODIS and *CALIPSO* using the 11- and 12-μm ACHA mode (used in Pv5.3) versus the 11- and 13.3-μm mode (used in Pv6.0) shows better accuracy and precision in the latter mode with improvement coming mostly in the vertical placement of ice phase clouds.

Pv6.0 shows decreases in intersatellite variability and seasonality in COD and an overall decrease in the median value. This can be attributed to more consistent cloud detection, an increase in the detection of thin clouds over ice-free oceans, and the removal of the 1.6-μm channel for use in the cloud mask. REF also shows minor improvement in intersatellite consistency though median values remain similar between Pv5.3 and Pv6.0. There is also a clear delineation between satellites that used the 1.6- versus 3.75-μm bands for DCOMP retrievals.

The creation of a long-term stable satellite record spanning 15 satellites necessitates making decisions about accuracy versus consistency. For Pv6.0 only channels available throughout the record were used for primary cloud retrievals. This is an example of favoring consistency over accuracy, though the analysis here suggests improvements in retrieval techniques and the addition of HIRS results in PV6.0 being both more accurate and consistent than Pv5.3. One question is whether spectral band adjustments will play a larger role in future versions of these records, and whether attempts to homogenize spectral information from multiple satellites through tuning could suppress or enhance climate signals. Other issues to be considered when using this record are the use of different surface types for training as this can introduce biases in interregional cloudiness, small shifts in SRFs between satellites, orbital drift, and inherent differences in uncertainty when detecting cloud in different conditions. It is hoped that the improvements shown in Pv6.0 will make it a more valuable record for use in climate applications, especially those that rely on intersatellite consistency.

Acknowledgments. This work was funded by a grant from the NOAA National Centers for Environmental Information. We would also like to thank Dr. Mark Kulie for his helpful comments and suggestions.

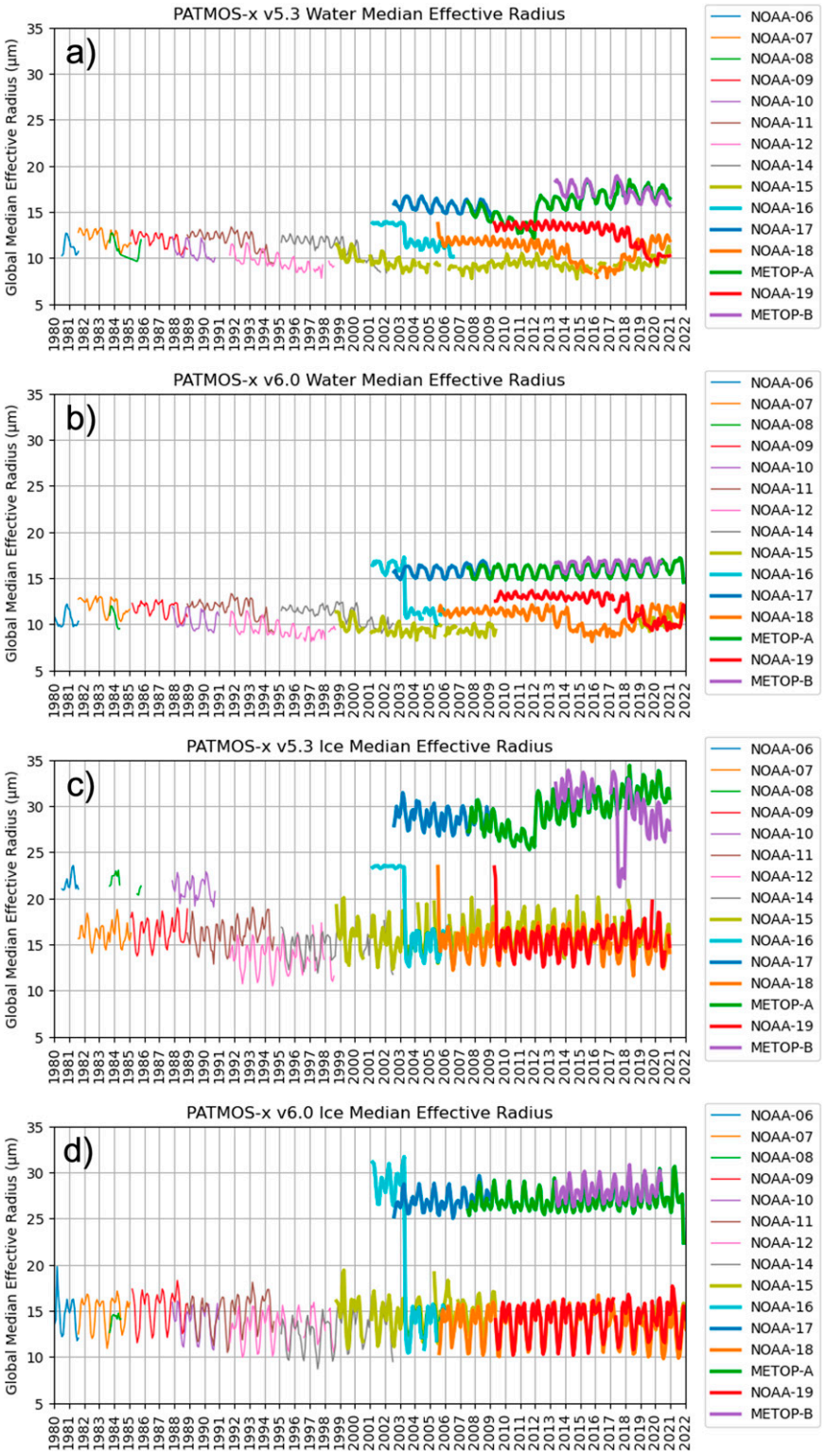

FIG. 10. Comparison of effective radius for Pv5.3 and Pv6.0. Time series of median effective radius are shown for (a) Pv5.3 water, (b) Pv6.0 water, (c) Pv5.3 ice, and (d) Pv6.0 ice.

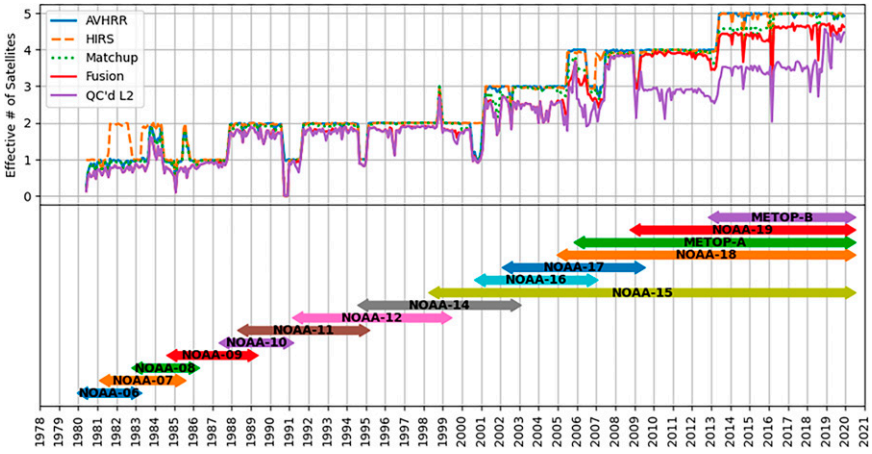

FIG. A1. Number of global overpasses available over the course of Pv6.0. Each satellite performs two global overpasses a day. The purple line represents the effective number of satellites available after checking the availability of AVHRR (blue line), HIRS (orange dashed line), successful matchup of the two (green dotted line), and successful running of the fusion process (red line).

Data availability statement. PATMOS-x v6.0 (Pv6.0) is available from NCEI at https://doi.org/10.7289/V5X9287S. Other datasets used in this analysis include the following:

CLDPROP_M3_VIIRS_SNPP: VIIRS/SNPP Cloud Properties Level 3 (https://ladsweb.modaps.eosdis.nasa.gov/missions-and-measurements/products/CLDPROP_M3_VIIRS_SNPP/);

Pv53: PATMOS-x v5.3 (http://doi.org/10.7289/V56W982J);

PxMOD: MODIS (*Aqua* and *Terra*) processed with current PATMOS-x software (can be made available upon request to the corresponding author);

MODIS_EOS: MODIS C6.1 (https://ladsweb.modaps.eosdis.nasa.gov/missions-and-measurements/products/MOD08_M3, https://ladsweb.modaps.eosdis.nasa.gov/missions-and-measurements/products/MYD08_M3/); and

CAL_LID_L3_GEWEX: CALIOP Cloud_Amount_Mean_Column from GEWEX (https://www-calipso.larc.nasa.gov/resources/calipso_users_guide/qs/cal_lid_l3_gewex_cloud_v1-00.php).

The backfitting code used to generate Fig. 6 can be found at https://gitlab.ssec.wisc.edu/cphillips/patmosx_tools.

APPENDIX A

Quality Assurance

A challenge with the historical AVHRR record is uneven sampling over time. Figure A1 shows that for much of the early record one or two satellites are available, while in the latter part has as many as five. Pv6.0 exacerbates this issue by placing additional constraints on radiometric input data. The requirement for Pv5.3 is valid AVHRR Global Area Coverage (GAC) data. For Pv6.0 there must also be valid HIRS Level 1b data. In addition, the start and end times for the AVHRR and HIRS overpasses must match (or be matched) and the fusion process, necessary to interpolate HIRS spectral information to AVHRR spatial resolution, must complete successfully. Figure A1 shows the effective number of satellites available after these quality assurance (QA) checks have been applied. The most significant difference in data availability between Pv5.3 and Pv6.0 occurs in the latter part of the record, where much of the *NOAA-15* record has been discarded due to a lack of valid HIRS data and the *MetOp-B* HIRS failed in mid-2020. The early part of the record is largely unchanged, which is fortunate as that is where the fewest number of satellites are available. The exception to this is the loss of *TIROS-N*, which flew from 1978 to 1981. Very few *TIROS-N* HIRS data were available during processing so it was determined *TIROS-N* did not meet QA requirements and was not included in the record.

APPENDIX B

Ancillary Data

Background atmospheric and surface state information is needed PATMOS-x processing that cannot be retrieved directly from the satellite imager measurements. This information can be broadly grouped into static data, which are the same throughout the record (e.g., topographical maps), and dynamic data that are periodically updated. The National Centers for Environmental Prediction (NCEP) generate a reanalysis product using the Climate Forecast System (CFS), which models interactions between the atmosphere, ocean, land, and cryosphere and assimilates observations from surface, radiosonde, aircraft, and satellite sources (Saha et al. 2010). The CFS reanalysis (CFSR) was originally generated from January 1979 to March 2011 and was later extended as an operational real-time product (Saha et al. 2014). The CFSR product used in PATMOS-x has a horizontal resolution of 0.5° and 26 vertical levels. The fields are available at 6-hourly intervals and interpolated to the scan line time from the AVHRR sensor. Several of the static fields are surface masks developed as part of the NOAA Global Land One-kilometer Base Elevation (GLOBE) Project. Table B1 lists the source and function of ancillary fields required for Pv6.0.

TABLE B1. Ancillary fields required for processing PATMOS-x.

Field name	Dimensions	Units	Function	Source	Temporal update frequency
Pressure levels	3D	hPa	Fixed levels used to ingest vertical profile fields	CFSR (Saha et al. 2010, 2014)	Static
Surface pressure	2D	hPa	Lowest pressure level over land given fixed vertical pressure profiles	CFSR (Saha et al. 2010, 2014)	Static
Mean sea level pressure	2D	hPa	Lowest pressure level over ocean given fixed vertical pressure profiles	CFSR (Saha et al. 2010, 2014)	Static
Surface temperature	2D	K	Surface boundary for RTM calculations	CFSR (Saha et al. 2010, 2014)	Every 6 h
Surface type	2D	—	Differentiates surface types for cloud mask training	UMD (Hansen et al. 1998, 2000)	Static
Surface elevation	2D	km	Interpolation of coarser-resolution ancillary fields to high-resolution topographic map	GLOBE Project (GLOBE Task Team et al. 1999)	Static
Land mask	2D	—	Differentiates surface types for cloud detection	GLOBE Project (GLOBE Task Team et al. 1999)	Static
Coast mask	2D	—	Differentiates land vs water surface types	GLOBE Project (GLOBE Task Team 1999)	Static
Total precipitable water	2D	cm	Atmospheric correction for visible absorption	CFSR (Saha et al. 2010, 2014)	Every 6 h
Water equivalent snow depth	2D	cm	Snow mask	CFSR (Saha et al. 2010, 2014)	Every 6 h
Tropopause temperature	2D	K	IR cloud detection	CFSR (Saha et al. 2010, 2014)	Every 6 h
Tropopause pressure	2D	hPa	IR cloud detection	CFSR (Saha et al. 2010, 2014)	Every 6 h
Temperature	3D	K	Vertical placement of cloud	CFSR (Saha et al. 2010, 2014)	Every 6 h
Height	3D	km	Vertical placement of cloud	CFSR (Saha et al. 2010, 2014)	Every 6 h
Ozone mixing ratio	3D	kg kg^{-1}	Atmospheric correction for visible absorption	CFSR (Saha et al. 2010, 2014)	Every 6 h
Relative humidity	3D	%	Atmospheric correction for radiative transfer calculations	CFSR (Saha et al. 2010, 2014)	Every 6 h
Sea surface temperature	2D	K	Surface boundary for RTM calculations	OISST	Daily
Surface albedo	2D	%	Surface correction for optical property retrieval	MODIS white-sky albedo (Moody et al. 2008)	Static (16-day climatology)
Surface emissivity	2D	%	Surface correction for radiative transfer calculations	SeeBor (Seemann et al. 2008)	Static (monthly climatology)

TABLE C1. Output fields introduced in PATMOS-x Version 6.0. Radiometric fields are HIRS measurements interpolated to the AVHRR pixel size and location as described in section 2c.

Field	Type	Description
hirsavhrr_total_precipitable_water	Product	Total column precipitable water
hirsavhrr_water_vapor_content_layerlow	Product	Atmospheric humidity (surface–680 hPa)
hirsavhrr_water_vapor_content_layermid	Product	Atmospheric humidity (680–440 hPa)
hirsavhrr_water_vapor_content_layerhigh	Product	Atmospheric humidity (<440 hPa)
temp_3_75um_nom_sounder	Radiometric	HIRS nominal 3.75-μm BT
temp_4_45um_nom_sounder	Radiometric	HIRS nominal 4.45-μm BT
temp_4_46um_nom	Radiometric	HIRS nominal 4.46-μm BT
temp_4_52um_nom	Radiometric	HIRS nominal 4.52-μm BT
temp_4_57um_nom_sounder	Radiometric	HIRS nominal 4.57-μm BT
temp_6_7um_nom	Radiometric	HIRS nominal 6.7-μm BT
temp_7_3um_nom	Radiometric	HIRS nominal 7.3-μm BT
temp_9_7um_nom	Radiometric	HIRS nominal 9.7-μm BT
temp_13_6um_nom	Radiometric	HIRS nominal 13.6-μm BT
temp_13_9um_nom	Radiometric	HIRS nominal 13.9-μm BT
temp_14_2um_nom	Radiometric	HIRS nominal 14.2-μm BT
temp_11_0um_nom_sounder	Radiometric	HIRS nominal 11.0-μm BT
temp_12_0um_nom_sounder	Radiometric	HIRS nominal 12.0-μm BT
temp_13_3um_nom_clear_sky	Radiometric	HIRS nominal clear-sky 13.3-μm BT
temp_13_3um_nom	Radiometric	HIRS nominal 13.2-μm BT
temp_14_5um_nom_sounder	Radiometric	HIRS nominal 14.5-μm BT
temp_14_7um_nom_sounder	Radiometric	HIRS nominal 14.7-μm BT
temp_14_9um_nom_sounder	Radiometric	HIRS nominal 14.9-μm BT
cld_temp_prior_acha	ACHA	Prior probability for height retrieval
prior_cloud_probability	Cloud mask	Prior probability for cloud detection
ice_cloud_probability	Cloud phase	Probability of cloud being ice phase
water_cloud_probability	Cloud phase	Probability of cloud being liquid phase
latitude_pc	Geolocation	Latitude adjusted for cloud parallax effect
longitude_pc	Geolocation	Longitude adjusted for cloud parallax effect
bayes_mask_sfc_type	Cloud mask	Surface type used for cloud mask
hirsavhrr_rtvl_qflag	Quality control	Water vapor quality control flags

APPENDIX C

Additional Output Fields

Several fields have been added to Pv6.0 output files, listed in Table C1. Besides HIRS radiometric information and TPW products several fields were added that were found to be useful for quality control and data analysis.

REFERENCES

Bony, S., and J. L. Dufresne, 2005: Marine boundary layer clouds at the heart of tropical cloud feedback uncertainties in climate models. *Geophys. Res. Lett.*, **32**, L20806, https://doi.org/10.1029/2005GL023851.

Borbas, E., S. W. Seemann, H.-L. Huang, J. Li, and W. P. Menzel, 2005: Global profile training database for satellite regression retrievals with estimates of skin temperature and emissivity. *Proc. 14th Int. ATOVS Study Conf.*, Beijing, China, 25–31 May 2005, 763–770, http://cimss.ssec.wisc.edu/training_data/data/itsc14_borbas_trainingData.pdf.

Boucher, O., and Coauthors, 2014: Clouds and aerosols. *Climate Change 2013: The Physical Science Basis*, T. F. Stocker et al., Eds., Cambridge University Press, 571–657.

Cracknell, A. P., 1997: *The Advanced Very High Resolution Radiometer (AVHRR)*. CRC Press, 556 pp.

Cross, J. I., I. Gladkova, W. P. Menzel, A. Heidinger, and M. D. Grossberg, 2013: Statistical estimation of a 13.3 μm visible infrared imaging radiometer suite channel using multisensor data fusion. *J. Appl. Remote Sens.*, **7**, 073473, https://doi.org/10.1117/1.JRS.7.073473.

Foster, M. J., and A. K. Heidinger, 2013: PATMOS-x: Results from a diurnally corrected 30-yr satellite cloud climatology. *J. Climate*, **26**, 414–425, https://doi.org/10.1175/JCLI-D-11-00666.1.

——, and ——, 2014: Entering the era of 30+ year satellite cloud climatologies: A North American case study. *J. Climate*, **27**, 6687–6697, https://doi.org/10.1175/JCLI-D-14-00068.1.

——, S. A. Ackerman, A. K. Heidinger, B. Maddux, and M. Stengel, 2014: Global cloudiness [in "State of the Climate in 2013"]. *Bull. Amer. Meteor. Soc.*, **95** (7), S22–S23, https://doi.org/10.1175/2014BAMSStateoftheClimate.1.

——, and Coauthors, 2019: Cloudiness [in "State of the Climate in 2018"]. *Bull. Amer. Meteor. Soc.*, **100** (9), S34–S35, https://doi.org/10.1175/2019BAMSStateoftheClimate.1.

GLOBE Task Team, and Coauthors, Eds., 1999: The Global Land One-kilometer Base Elevation (GLOBE) digital elevation model, version 1.0. NOAA, National Geophysical Data Center, accessed October 2019, https://www.ngdc.noaa.gov/mgg/topo/globe.html.

Hansen, M., R. DeFries, J. R. G. Townshend, and R. Sohlberg, 1998: UMD Global Land Cover Classification, 1 Kilometer, 1.0.

Department of Geography, University of Maryland, 1981–1994, https://app.earth-observer.org/data/basemaps/images/global/LandCover_512/LandCoverUMD_512/LandCoverUMD_512.html.

——, ——, ——, and ——, 2000: Global land cover classification at 1 km resolution using a decision tree classifier. *Int. J. Remote Sens.*, **21**, 1331–1365, https://doi.org/10.1080/014311600210209.

Heidinger, A. K., and M. J. Pavolonis, 2009: Gazing at cirrus clouds for 25 years through a split-window. Part I: Methodology. *J. Appl. Meteor. Climatol.*, **28**, 1100–1116, https://doi.org/10.1175/2008JAMC1882.1.

——, C. Cao, and J. T. Sullivan, 2002: Using Moderate Resolution Imaging Spectrometer (MODIS) to calibrate advanced very high resolution radiometer reflectance channels. *J. Geophys. Res.*, **107**, 4702, https://doi.org/10.1029/2001JD002035.

——, W. C. Straka, C. C. Molling, J. T. Sullivan, and X. Q. Wu, 2010: Deriving an inter-sensor consistent calibration for the AVHRR solar reflectance data record. *Int. J. Remote Sens.*, **31**, 6493–6517, https://doi.org/10.1080/01431161.2010.496472.

——, M. J. Foster, and A. T. Evan, 2012: A CALIPSO derived naive Bayesian cloud detection scheme for the Pathfinder Atmospheres Extended (PATMOS-x) data set. *J. Appl. Meteor. Climatol.*, **51**, 1129–1144, https://doi.org/10.1175/JAMC-D-11-02.1.

——, ——, A. Walther, and X. Zhao, 2014: The Pathfinder Atmospheres Extended (PATMOS-x) AVHRR climate data set. *Bull. Amer. Meteor. Soc.*, **95**, 909–922, https://doi.org/10.1175/BAMS-D-12-00246.1.

——, and Coauthors, 2019: Using sounder data to improve cirrus cloud height estimation from satellite imagers. *J. Atmos. Oceanic Technol.*, **36**, 1331–1342, https://doi.org/10.1175/JTECH-D-18-0079.1.

Ignatov, A., I. Laszlo, E. D. Harrod, K. B. Kidwell, and G. P. Goodrum, 2004: Equator crossing times for NOAA, ERS and EOS sun-synchronous satellites. *Int. J. Remote Sens.*, **25**, 5255–5266, https://doi.org/10.1080/01431160410001712981.

Karlsson, K.-G., and A. Devasthale, 2018: Inter-comparison and evaluation of the four longest satellite-derived cloud climate data records: CLARA-A2, ESA Cloud CCI V3, ISCCP-HGM, and PATMOS-x. *Remote Sens.*, **10**, 1567, https://doi.org/10.3390/rs10101567.

Klein, S. A., A. Hall, J. R. Norris, and R. Pincus, 2017: Low-cloud feedbacks from cloud-controlling factors: A review. *Surv. Geophys.*, **38**, 1307–1329, https://doi.org/10.1007/s10712-017-9433-3.

Liu, Y., J. R. Key, R. A. Frey, S. A. Ackerman, and W. P. Menzel, 2004: Nighttime polar cloud detection with MODIS. *Remote Sens. Environ.*, **92**, 181–194, https://doi.org/10.1016/j.rse.2004.06.004.

Menzel, W. P., and Coauthors, 2008: MODIS global cloud-top pressure and amount estimation: Algorithm description and results. *J. Appl. Meteor. Climatol.*, **47**, 1175–1198, https://doi.org/10.1175/2007JAMC1705.1.

Moody, E. G., M. D. King, C. B. Schaaf, and S. Platnick, 2008: MODIS-derived spatially complete surface albedo products: Spatial and temporal pixel distribution and zonal averages. *J. Appl. Meteor. Climatol.*, **47**, 2879–2894, https://doi.org/10.1175/2008JAMC1795.1.

Nakajima, T., and M. D. King, 1990: Determination of the optical thickness and effective particle radius of clouds from reflected solar radiation measurements. Part I: Theory. *J. Atmos. Sci.*, **47**, 1878–1893, https://doi.org/10.1175/1520-0469(1990)047<1878:DOTOTA>2.0.CO;2.

Nielsen, J. K., M. Foster, and A. Heidinger, 2011: Tropical stratospheric cloud climatology from the PATMOS-x dataset: An assessment of convective contributions to stratospheric water. *Geophys. Res. Lett.*, **38**, L18801, https://doi.org/10.1029/2011GL049429.

Platnick, S., and Coauthors, 2015: MODIS atmosphere L3 monthly product. NASA MODIS Adaptive Processing System, Goddard Space Flight Center, accessed February 2022, https://doi.org/10.5067/MODIS/MOD08_M3.061.

——, and Coauthors, 2019: VIIRS atmosphere L3 cloud properties product, version-1.1. NASA Level-1 and Atmosphere Archive & Distribution System (LAADS) Distributed Active Archive Center (DAAC), Goddard Space Flight Center, accessed February 2022, https://doi.org/10.5067/VIIRS/CLDPROP_M3_VIIRS_SNPP.011.

Rausch, J., A. Heidinger, and R. Bennartz, 2010: Regional assessment of microphysical properties of marine boundary layer cloud using the PATMOS-x dataset. *J. Geophys. Res.*, **115**, D23212, https://doi.org/10.1029/2010JD014468.

Rodgers, C. D., 1976: Retrieval of atmospheric temperature and composition from remote measurements of thermal radiation. *Rev. Geophys.*, **14**, 609–624, https://doi.org/10.1029/RG014i004p00609.

Saha, S., and Coauthors, 2010: The NCEP Climate Forecast System Reanalysis. *Bull. Amer. Meteor. Soc.*, **91**, 1015–1058, https://doi.org/10.1175/2010BAMS3001.1.

——, and Coauthors, 2014: The NCEP Climate Forecast System version 2. *J. Climate*, **27**, 2185–2208, https://doi.org/10.1175/JCLI-D-12-00823.1.

Saunders, R., and Coauthors, 2018: An update on the RTTOV fast radiative transfer model (currently at version 12). *Geosci. Model Dev.*, **11**, 2717–2737, https://doi.org/10.5194/gmd-11-2717-2018.

Scarino, B., D. R. Doelling, P. Minnis, A. Gopalan, T. L. Chee, R. Bhatt, C. Lukashin, and C. Haney, 2016: A web-based tool for calculating spectral band difference adjustment factors derived from SCIAMACHY hyperspectral data. *IEEE Trans. Geosci. Remote Sens.*, **54**, 2529–2542, https://doi.org/10.1109/TGRS.2015.2502904.

Seemann, S. W., J. Li, W. P. Menzel, and L. E. Gumley, 2003: Operational retrieval of atmospheric temperature, moisture, and ozone from MODIS infrared radiances. *J. Appl. Meteor.*, **42**, 1072–1091, https://doi.org/10.1175/1520-0450(2003)042<1072:OROATM>2.0.CO;2.

——, E. E. Borbas, R. O. Knuteson, G. R. Stephenson, and H.-L. Huang, 2008: Development of a global infrared emissivity database for application to clear sky sounding retrievals from multi-spectral satellite radiances measurements. *J. Appl. Meteor. Climatol.*, **47**, 108–123, https://doi.org/10.1175/2007JAMC1590.1.

Sengupta, M., Y. Xie, A. Lopez, A. Habte, G. Maclaurin, and J. Shelby, 2018: The National Solar Radiation Data Base (NSRDB). *Renew. Sustainable Energy Rev.*, **89**, 51–60, https://doi.org/10.1016/j.rser.2018.03.003.

Stubenrauch, C. J., and Coauthors, 2012: Assessment of global cloud datasets from satellites: Project and database initiated by the GEWEX radiation panel. *Bull. Amer. Meteor. Soc.*, **94**, 1031–1049, https://doi.org/10.1175/BAMS-D-12-00117.1.

Walther, A., and A. K. Heidinger, 2012: Implementation of the Daytime Cloud Optical and Microphysical Properties algorithm (DCOMP) in PATMOS-x. *J. Appl. Meteor. Climatol.*, **51**, 1371–1390, https://doi.org/10.1175/JAMC-D-11-0108.1.

Weisz, E., B. A. Baum, and W. P. Menzel, 2017: Fusion of satellite-based imager and sounder data to construct supplementary high spatial resolution narrowband IR radiances. *J. Appl. Remote Sens.*, **11**, 036022, https://doi.org/10.1117/1.JRS.11.036022.

Winker, D. M., M. A. Vaughan, A. Omar, Y. Hu, K. A. Powell, Z. Liu, W. H. Hunt, and S. A. Young, 2009: Overview of the CALIPSO mission and CALIOP data processing algorithms. *J. Atmos. Oceanic Technol.*, **26**, 2310–2323, https://doi.org/10.1175/2009JTECHA1281.1.

Wu, D. L., and Coauthors, 2017: Toward global harmonization of derived cloud products. *Bull. Amer. Meteor. Soc.*, **98**, ES49–ES52, https://doi.org/10.1175/BAMS-D-16-0234.1.

Wu, W., Y. Liu, M. P. Jensen, T. Toto, M. J. Foster, and C. N. Long, 2014: A comparison of multiscale variations of decade-long cloud fractions from six different platforms over the southern Great Plains in the United States. *J. Geophys. Res. Atmos.*, **119**, 3438–3459, https://doi.org/10.1002/2013JD019813.

Zelinka, M. D., C. Zhou, and S. A. Klein, 2016: Insights from a refined decomposition of cloud feedbacks. *Geophys. Res. Lett.*, **43**, 9259–9269, https://doi.org/10.1002/2016GL069917.

Zhang, B., C. Cao, T.-C. Liu, and X. Shao, 2021: Spectral recalibration of NOAA HIRS longwave CO_2 channels toward a 40+ year time series for climate studies. *Atmosphere*, **12**, 1317, https://doi.org/10.3390/atmos12101317.

Zhao, T. X.-P., P. K. Chan, and A. K. Heidinger, 2013: A global survey of the effect of cloud contamination on the aerosol optical thickness and its long-term trend derived from operational AVHRR satellite observations. *J. Geophys. Res. Atmos.*, **118**, 2849–2857, https://doi.org/10.1002/jgrd.50278.

Zhong, Y., M. Notaro, S. J. Vavrus, and M. J. Foster, 2016: Recent accelerated warming of the Laurentian Great Lakes: Physical drivers. *Limnol. Oceanogr.*, **61**, 1762–1786, https://doi.org/10.1002/lno.10331.